

Seismic methods for fluid discrimination in areas with complex geologic history — A case example from the Barents Sea

Ivan Lehocki¹, Per Avseth², and Nazmul Haque Mondol³

Abstract

We have developed a new scheme for calculation of density ratio, an attribute that can be directly linked to hydrocarbon saturation, and applied it to seismic amplitude variation with offset (AVO) data from the Hoop area in the Barents Sea. The approach is based on the inversion of Zoeppritz's equation for PP-wave. Furthermore, by using interval velocities, we quantified uplift magnitude for a given interval beneath Base Cretaceous unconformity (BCU) horizon in the Hoop area. Depending on the temperature gradient, the maximum burial depth can be estimated, a crucial factor affecting the elastic properties of the rocks. Coupling uplift map with temperature history for key stratigraphic units from basin modeling enabled us to extend the training data away from well control. By doing so, we created nonstationary AVO probability density functions (PDFs) for calibration and classification of seismic attributes in the test area. This decreases the likelihood of misclassification of pore fluid type as opposed to the case where the training data are created based only on sparse well-log data. We tested and compared the methods on the Barents Sea seismic data set, and the results were validated at four well locations. Finally, maps of fluid distribution obtained from stochastic rock-physics modeling honoring burial history were compared against the density ratio map. Four maps revealed the same anomalous zones, the major difference being the detection of the down-flank presence of oil associated with some of the predicted gas anomalies in the prospect area, in the case of density ratio map. Possible gas caps were detected/predicted only for certain temperature constraints during the AVO classifications and were most obvious in the density ratio map.

Introduction

A holy grail of quantitative seismic interpretation is to obtain accurate pore fluid predictions. This task is increasing in complexity as the undetected hydrocarbon traps are more subtle than before. Their discovery demands new and improved measurement techniques, novel workflows, and robust algorithms for coupling and integrating (e.g., well log, seismic, electromagnetic, gravity) data, as well as more sophisticated methods that bridge the gaps between geophysics and geology, traditionally viewed as separate disciplines (e.g., basin and rock physics modeling). A prospective area in the Barents Sea that has been chosen for this study (Figure 1) exhibits regional and temporal geologic complexity, meaning that the rocks in some regions can be subjected to several episodes of subsidence, uplift, and erosion over the geologic time. One formation that holds record of such processes is the Stø Formation (Fm), known to be the most important reservoir sand(stone) in the southwestern Barents Sea (Farazani, 2017). Stø Fm sand(stone)s were deposited in the

Middle Jurassic time period as shallow marine sands in a coastal environment. They have been buried deeper (>1500–2000 m) and later uplifted to a shallow depth (a few hundred meters) in the Hoop area. The active tectonic history of the area may induce anisotropy in elastic parameters (Veire et al., 2016), especially in the shallow overburden (Lewis et al., 2016), as is the case in the area of our investigation. This anisotropy could be associated with intrinsic layering in the shale overburden, as well as cracks and/or stress anisotropy associated with the unloading. If anisotropy is not accounted for, uncertainty is added to calculations, which will inevitably distort the (inversion) results. The simple way we fudge the elastic anisotropy of shales is through the process of seismic calibration, that is, when bringing seismic amplitudes to reflectivity domain. Although mathematically not rigorous, this simple step seems to be sufficient for obtaining reliable fluid maps.

It is well-known that the initial cementation (a small amount of cement) drastically stiffens the rock frame,

¹Lehocki GeoSpace, Oslo, Norway. E-mail: lehocki@geospace.no.

²Dig Science, Oslo, Norway and Norwegian University of Science and Technology (NTNU), Department of Geoscience and Petroleum, Trondheim, Norway. E-mail: per.avseth@digscience.no.

³University of Oslo, Department of Geosciences, Oslo, Norway and Norwegian Geotechnical Institute (NGI), Oslo, Norway. E-mail: m.n.h.mondol@geo.uio.no; nhm@ngi.no.

Manuscript received by the Editor 12 April 2019; revised manuscript received 10 August 2019; published ahead of production 16 September 2019; published online 21 January 2020. This paper appears in *Interpretation*, Vol. 8, No. 1 (February 2020); p. SA35–SA47, 12 FIGS., 2 TABLES.

<http://dx.doi.org/10.1190/INT-2019-0057.1>. © 2020 Society of Exploration Geophysicists and American Association of Petroleum Geologists. All rights reserved.

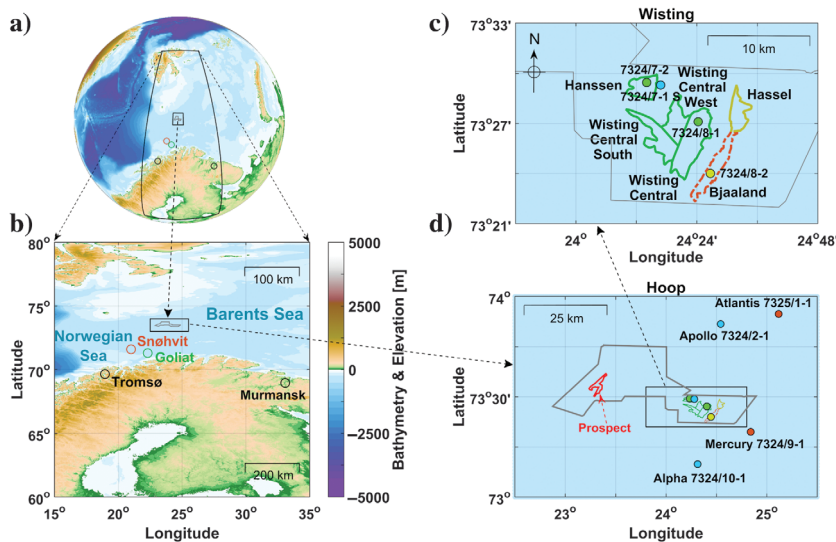


Figure 1. Maps of the study area. Panel (a) gives a global perspective of the location of the study area (marked by a small black polygon, i.e., the spherical rectangle), and (b) shows a magnified, regional map, where major discoveries, namely, Snøhvit and Goliat, are also displayed. The black rectangle in this subplot is further magnified to display the local map of the study area in the SW Barents Sea, namely, Hoop, seen in (d). The gray polygon marks the area within which the seismic data for the interface under scope are at disposal. The location of the prospective area is highlighted by a red contour box. Wells are colored to reflect the fluid content found in the Stø Formation at the time of drilling. The color code is as follows: cyan — dry well (brine), green — hydrocarbon discovery (oil), dark red — hydrocarbon discovery (gas), and yellow — subcommercial gas find (approximately 10%–20% gas + 80%–90% brine mixture). Four wells (7324/7-1 S [Wisting Alternative], 7324/7-2 [Hanssen], 7324/8-1 [Wisting Central], and 7324/8-2 [Bjaaland]) used in this study are from the Wisting discovery. As (c) reveals, the Wisting structure is divided into six segments and each segment is color-coded according to the HC content: Wisting Central, Wisting Central West, Wisting Central South, and Hanssen are all oil discoveries, Bjaaland is a residual gas discovery, and Hassel is a prospect yet to be drilled. The same color bar with the same limits as shown in (b) applies to (a, c, and d). Bathymetry and elevation data are obtained from the National Oceanic and Atmospheric Administration.

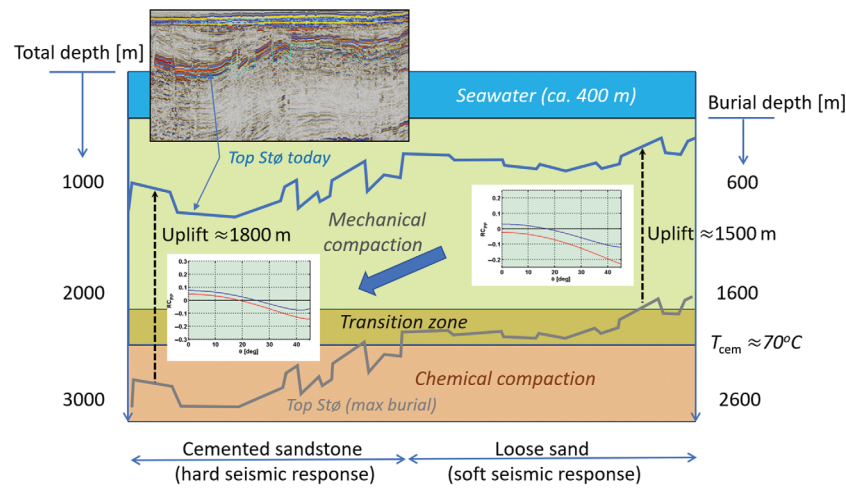


Figure 2. Schematic illustration of the burial history profile along a random seismic line in the Hoop area, showing the present and maximum burial of the Top Stø Fm. The AVO signatures (and fluid sensitivities) will vary as a function of burial depth (the blue AVO curves represent the water case, and the red curves represent the gas case).

which in turn significantly decreases the fluid sensitivity and thus makes the task of inverting for pore fluids from seismic data alone very difficult (e.g., Dræge et al., 2014). Adding more cement to the rock only worsens the situation. Consequently, accurate fluid discrimination may seem like an insurmountable task. Therefore, the classically derived attributes developed for fluid distinction have to be used with great caution.

Avseth et al. (2003) introduced a statistical AVO fluid discrimination, which honors rock-physics depth trends. This approach works well in areas with fairly simple tectonic history. Then, to comply with more complex cases of the local/regional basin evolution, Avseth and Lehocki (2016) took the method one step further by linking burial history and rock-physics modeling of shales and sands. This allowed for the creation of training data obeying complex geologic record of time-temperature relationship for the wells under the scope. These training data could then be used as inputs to fluid classification algorithms. However, the conditions that are valid at and in the vicinity of one well may not be representative of the conditions encountered elsewhere in the area of investigation, as revealed in Figure 2. Therefore, it is a necessary step to extend the training data away from well control.

A more robust workflow for obtaining the most likely fluid distribution map of the target reservoir sandstones was suggested by Lehocki et al. (2018). The core idea is to directly invert Zoeppritz's equation for PP-waves to obtain the density ratio, an attribute one simple algebraic step away from obtaining bulk densities at the top of the reservoir zone. Such information, much less affected by the initial contact stiffening diagenesis, can not only provide us with an accurate spatial distribution of hydrocarbon accumulation, but it also has the potential of discerning subtle differences in commercial versus noncommercial gas accumulations.

The purpose of this study was threefold:

- 1) Create an accurate map of the fluid distribution at the shale-sand(stone) interface in the area with complex tectonic history by application of two novel methods.

- 2) Compare fluid maps obtained by the two new methods with each other and the fluid map calculated with the classification methodology suggested by [Avseth and Lehocki \(2016\)](#).
- 3) Choose the best method consistent with all of the observations (from the well data), which also has the potential to discriminate between commercial and noncommercial gas accumulations.

The three techniques were applied to the Fuglen shale (cap rock) — Stø sand(stone) (reservoir rock) interface in the Wisting area in the Barents Sea where log data from four exploration wells served as checkpoints (the upper right subplot in Figure 1). More generally, they were applied to Hoop area to shed light on the most likely type of fluid residing in the pores of the anomalous prospect area.

The structure of the paper is as follows: first, the technical aspects of the seismic methods for fluid classification used in this paper are described. This is followed by a case study example from the Barents Sea, where the subtle, yet important, differences in fluid maps calculated by the three different methods are revealed and discussed. Finally, the concluding remarks are summarized in the “Conclusion” section.

Seismic methods for fluid classification

Method 1 — Fluid classification with stationary AVO PDFs

A great variety of attributes can be derived from pre-stack seismic data. Those developed to be sensitive to pore fluid changes, such as the widely used fluid factor ([Smith and Gidlow, 1987](#)), serve as great tools for initial screening through the AVO attributes to identify anomalous regions. The potential pitfalls, especially in areas with complex tectonic history, are twofold: either a water-saturated rock or a noncommercial hydrocarbon accumulation can be falsely identified as prospective anomalies, or hidden traps not easily detected on classic fluid-sensitive attributes, may stay unspotted.

To decrease the likelihood of either of these pitfalls, [Avseth and Lehocki \(2016\)](#) introduced a workflow that combines the temperature history and rock-physics modeling of shales and sand(stone)s to calculate the expected seismic responses in two hydrocarbon fields. Although more sophisticated than previous methods, their approach did not account for lateral changes in the present burial depth of the formation under the scope. More importantly, it did not attempt to estimate the maximum burial depth of the sand(stone)s investigated. Essentially, the silent assumption was that the AVO training data created by honoring the temperature history at one well location apply to the whole field. This assumption is wrong in more cases than not, and can lead to subtle, yet important, changes in statistical classification of the most likely fluid class, depending on the degree of difference in the lateral variation of the maximum burial depth (see Figure 2). This is particularly relevant if we screen for AVO anomalies near

the transition between the mechanical and chemical compaction domains.

The workflow suggested by [Avseth and Lehocki \(2016\)](#) was repeated in this paper. As the first step, time-temperature relationships for different formations found in the Wisting Central well (7324/8-1) were obtained from the in-house basin modeling performed by MOECO, Norway (the upper left subplot in Figure 3). Then, the relationship for the Top Stø Fm, the primary focus of our work, was transformed into burial history curves (BHCs) for two temperature gradient scenarios (as seen in the lower left subplot of Figure 3). A simple, linear, time-invariant relationship between the temperature and depth increase is assumed to hold true:

$$T(z_{\text{BD}}) = T_{\text{grad}} \cdot (z_{\text{BD}} - z_0) + T_0, \quad (1)$$

where z_{BD} is the burial depth (BD) [m], $z_0 = 0$ m, $T(z_{\text{BD}})$ is the temperature valid at a given burial depth, and $T_0 = T(z_0) = T_{\text{SB}}(t)$ is the sea-bottom (or surface) temperature [$^{\circ}\text{C}$] at the time when the formation enters cementation window. The cement precipitation is assumed to initiate at $T_{\text{cem}} = 70^{\circ}\text{C}$ ([Bjørlykke, 1998](#)).

In sedimentary basins with normal geothermal gradients ($\approx 33^{\circ}\text{C}/\text{km}$), such as the North Sea, the cementation onset is found at approximately 2000 m burial depth (assuming $T_{\text{SB}} = 4^{\circ}\text{C}$). A closer inspection of the upper left subplot in Figure 3 found on the right shows that Stø Fm first “touched” the cementation onset boundary approximately 40 million years ago when the sea-bottom temperature was 15°C . At spacetime point 1, the cementation onset was 1447 m, given the temperature gradient of $38^{\circ}\text{C}/\text{km}$. Ten million years later, the Barents Sea bottom temperature has cooled down to approximately 5°C . Repeating the calculation with this value would set the cementation line to 1711 m burial depth. This is only 52 m shallower than the maximum burial depth of the Stø Fm from $T_{\text{grad}} = 38^{\circ}\text{C}/\text{km}$ case (the orange circle in the lower left subplot). As shown in the time-dependent rock-physics modeling of the Wisting Central well in Figure 4, the velocities at the Top Stø Fm observed today can be explained if the rock has spent a longer time in the cementation window and hence obtained a larger cement volume. Furthermore, the choice of $T_{\text{grad}} = 38^{\circ}\text{C}/\text{km}$ transforms the Time-T curves into BHCs that almost perfectly explain the present burial depth of the Top Stø sandstones (237 and 239 m, respectively). The choice of this gradient as an average input in our calculations for the whole area of research is backed by [Khutorskoi et al. \(2008\)](#), who report a higher-than-average temperature gradient interval expected to be encountered beneath the Barents Sea basin ($35^{\circ}\text{C}/\text{km} - 42^{\circ}\text{C}/\text{km}$), based on their geothermal modeling. It should be noted, however, that the temperature gradient can change significantly in time and space in the Barents Sea, associated with complex tectonics and repeated exhumation episodes (e.g., [Zattin et al., 2016](#)), and therefore it represents a key uncertainty in the combined burial history and rock physics.

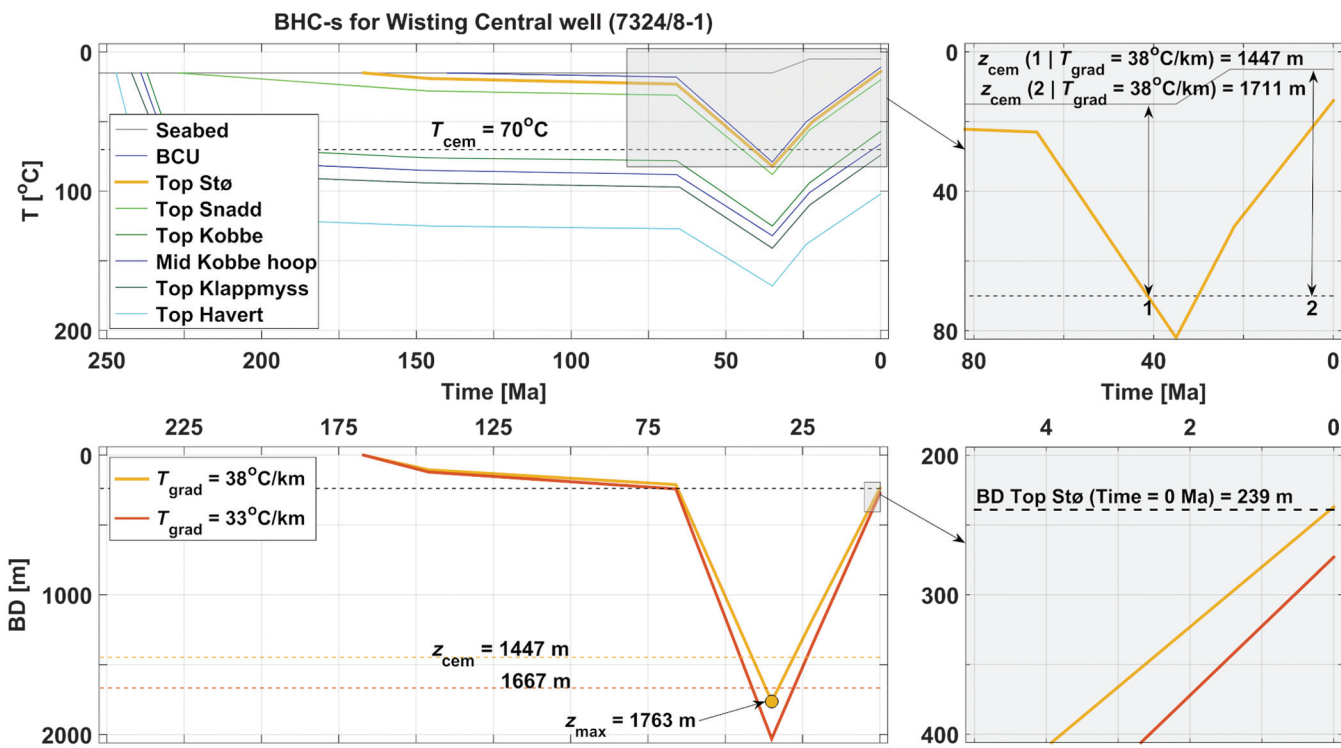


Figure 3. Temperature history curves for different formations encountered in the Wisting Central well (the upper left subplot). Corresponding BHCs for the Top Stø Fm for two temperature gradient scenarios are shown on the lower left subplot. The shaded areas in both subplots are magnified and shown in the subplots on the right. Note that the present burial depth of the Top Stø Fm matches the BHC calculated with $T_{\text{grad}} = 38^\circ\text{C}/\text{km}$ (the lower right subplot).

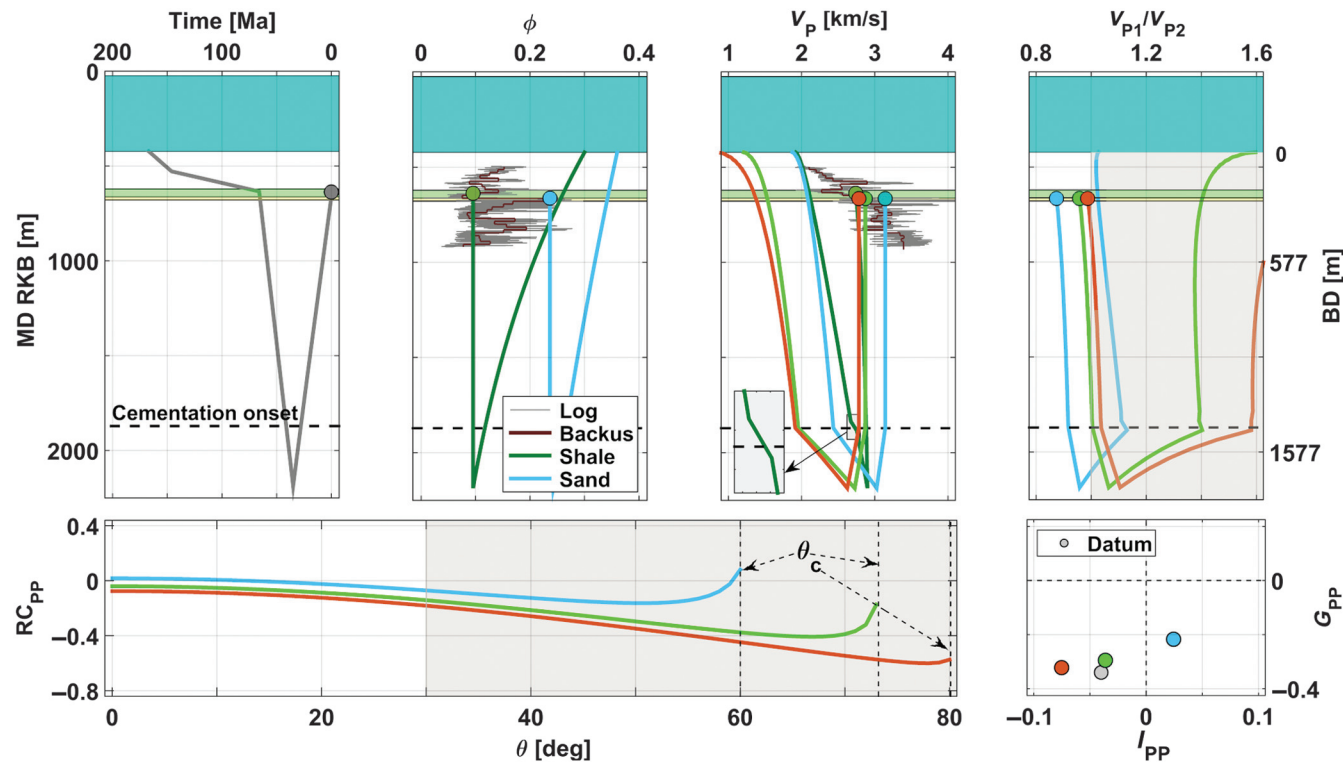


Figure 4. Rock-physics time trend modeling constrained by the BHCs (top row) and the corresponding amplitude variation with angle (AVA) response for the Wisting Central well (7324/8-1). The color code of the rock physics models is as follows: dark green — shale, cyan — brine-saturated sand(stone), green — oil-saturated sand(stone), and red — gas-saturated sand(stone).

Next, a time trend modeling was performed for the Wisting Central well as shown in Figure 4. The rocks in the area are known to have been subjected to several uplift episodes and the reservoir rock entered the quartz cementation window (denoted by the dashed lines in the top row of subplots in Figure 4) at this particular well location some 40 million years ago. The temperature history information is encoded into the BHC (the upper left subplot) and is essential in matching well-log observations and predicting correct seismic signatures. More closely, it allows for quantitative tracing of the evolution of the rock-physics properties in time and depth. In subplots 2 and 3, porosities and velocities at the target level are matched with Backus upscaled logs. A small part in subplot 3 is magnified into the shale model and shows the interval of velocity increase due to the temperature-induced chemical transition of smectite-rich to illite-rich shales. This transition kicks in at approximately 70°C–80°C (e.g., Børlykke, 2015). In subplot 4, the V_{P1}/V_{P2} ratios for different fluids are traced “from cradle to grave,” where V_{P1} and V_{P2} denote the velocities in the Fuglen Fm shales (top) and Stø Fm sand(stone)s (bottom), respectively.

At time = 0 Ma, i.e., present-day burial, the three modeled fluid scenarios exhibit class IIp (brine) and class III responses (oil and gas), as shown in the I_{PP} - G_{PP} crossplot in Figure 4, where G_{PP} denotes gradient term in the Shuey three-term fit approximation of the P-to-P Zoeppritz equation. The corresponding reflection coefficient curves have critical angles of approximately 60° for brine, 73° for oil, and 80° for gas case (the lower left subplot). Note that the lower left subplot has been shaded from the incident angle of 30° onward to illustrate that this angle range is usually unavailable in the prestack AVA/AVO analysis.

Method 2 — Fluid classification with nonstationary AVO PDFs

Whereas the rock-physics depth trends modeling suggested by Avseth et al. (2003) provides a robust approach to model basins with continuous subsidence or

simple tectonic history, the use of geologic time trends (i.e., BHCs) is crucial for tracking the time evolution of elastic properties of siliciclastic rocks. Only by doing so do we have a chance of getting a good understanding of the presently observed seismic signatures.

To be able to perform the calculations with this method without using the full basin modeling (i.e., without considering the whole thermal history of the basin), we need to make several assumptions. The first one is to set an average, constant, i.e., time-invariant and linear temperature gradient (equation 1). Then, taking the BHC from the Wisting Central well as the starting point, i.e., the guiding curve, we furthermore assume that all of the Stø Fm sand(stone)s in the area (presently found at our target interface) have been following the same time-depth trajectory from their deposition in Middle Jurassic to a steeper subsidence onset initiated in the Paleocene epoch (the middle subplot in Figure 5). This assumption translates into saying that the shape of BHCs at any spatial point before the Paleocene subsidence onset is not important from the perspective of fluid classification. What is important is the estimation of the maximum burial depth of the Top Stø Fm because it may have a major impact on the results of fluid classification. From the steeper subsidence point on, the BHCs start to diverge from the guiding BHC and need to be updated/corrected for the present and maximum burial depths. The Fuglen Fm, representing a transgressive shale and a regional cap rock, is assumed to have the same burial history as the Stø Fm reservoir sand(stone)s. To estimate the maximum burial depth of the target interface between Base Fuglen and Top Stø, we quantify the uplift from interval velocities estimated from the stacking velocity data. This technique is well known and has been used frequently on the Norwegian shelf to create net uplift maps (e.g., Henriksen et al., 2011; Baig et al., 2016; Gateman and Avseth, 2016; Johansen et al., 2017). Normally, Kolmule shales serve as the optimal zone to perform net uplift estimates in

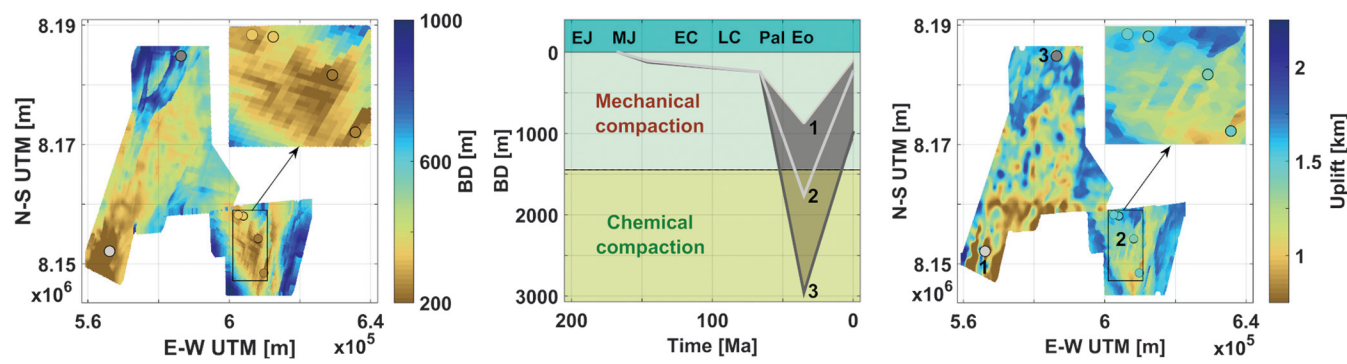


Figure 5. Present burial depth (left) and uplift (right) maps for the Top Stø Fm sand(stone)s. The middle subplot shows the BHCs for each spatial point in the maps. In addition, the present average seawater thickness of approximately 400 m (to scale) in the southwestern Barents Sea is highlighted by the cyan color. Curves 1, 2, and 3, which correspond to the spatial points (on maps) with the smallest maximum burial (southwest Hoop), the Wisting Central well, and the spatial point with the largest maximum burial depth (northern Hoop), respectively, are highlighted in the middle subplot, and their spatial locations are shown in the left and right subplots. The notation in the middle subplot denotes the following geologic epochs: EJ — Early Jurassic, MJ — Middle Jurassic, EC — Early Cretaceous, LC — Late Cretaceous, Pal — Paleocene, and Eo — Eocene.

the Barents Sea, given that the Kolmule shales are often very clay-rich. However, they show a varying lithology in the area of interest, and the interval velocities of the thin, shallow Kolmule interval are not reliable; thus, we have decided to use the interval beneath the BCU to establish relative uplift trends, and then these trends have been calibrated with uplift estimates at well locations.

By combining uplift and present-day burial depth maps, the last two points of BHCs are obtained for each spatial location. Effectively, we extend the training data away from the well control, and assuming a constant temperature gradient and setting a cementation onset value to $T_{\text{cem}} = 70^\circ\text{C}$, we can assess the degree of consolidation of the Stø Fm spatially away from well control. This is essential information for qualitative and quantitative assessment of pore sensitivity to fluid change in sand (stone)s. Then, these BHCs are used to guide the creation of AVO PDFs, which opens up the possibility to perform a fluid classification with locally adjusted, nonstationary, i.e., maximum burial-depth-corrected AVO PDFs (see Al-kawai et al., 2018). The method is a continuation of the methodology suggested by Avseth and Lehooki (2016).

We tested two scenarios to assess the effect of varying temperature gradient on calculated reservoir properties, such as cement volume and porosity shown in Figure 6. The upper subplots represent the $T_{\text{grad}} = 33^\circ\text{C}/\text{km}$ scenario (case 1), and the lower subplots represent the $T_{\text{grad}} = 38^\circ\text{C}/\text{km}$ (case 2). The comparison reveals that the rocks are less cemented and more porous in case 1. Rock physics diagnostics at four well locations indicate

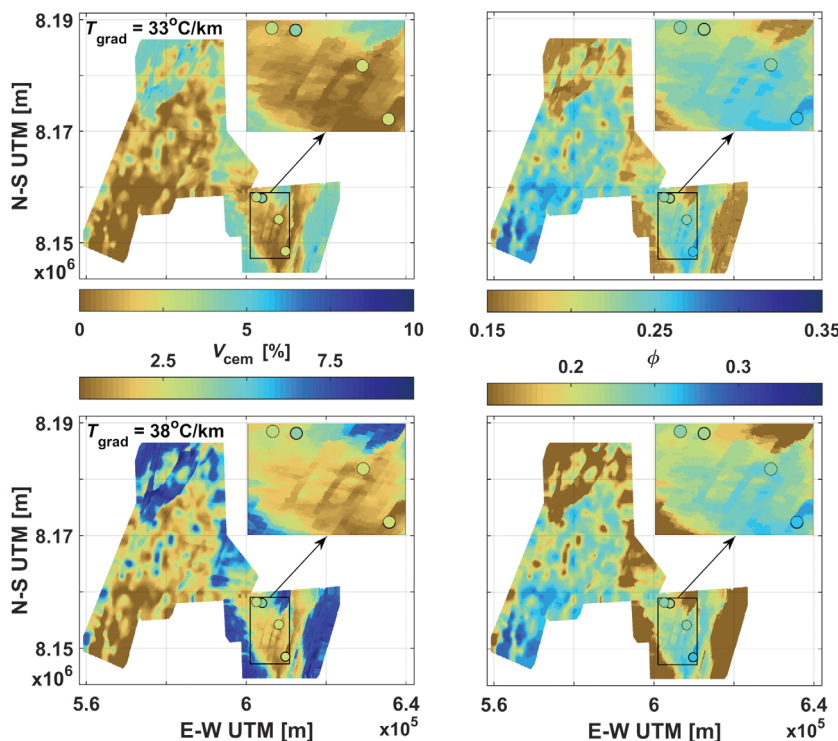


Figure 6. Cement volume and total porosity maps for $T_{\text{grad}} = 33^\circ\text{C}/\text{km}$ (the upper subplots) and $T_{\text{grad}} = 38^\circ\text{C}/\text{km}$ scenarios.

1%–3% quartz cement in the Stø Fm in the Wisting area. The $T_{\text{grad}} = 38^\circ\text{C}/\text{km}$ shows the more realistic, slightly cemented Wisting area, albeit with a little lower cement volume than at well locations. Note that a large part of the Hoop area along the southwest–northeast direction has $V_{\text{CEM}} = 0\%$ or close to 0% in case 1, indicating unconsolidated sands. In contrast, only sands in the southwest Hoop seem not to have entered the cementation window for the $T_{\text{grad}} = 38^\circ\text{C}/\text{km}$ case.

We continue investigating the effect on calculations caused by the two gradient scenarios, this time on elastic properties. Again, the $T_{\text{grad}} = 33^\circ\text{C}/\text{km}$ case is plotted in the upper subplots, and the $T_{\text{grad}} = 38^\circ\text{C}/\text{km}$ case is plotted in the lower subplots in Figures 7 and 8, respectively. Differences for the Fuglen shales are subtle, but the V_P velocities in scenario 2 seem to match slightly better the values at well locations (compare the magnified plots in the leftmost subplots of Figure 7). One probable reason for such similarity is that the model used in our calculations fails to properly capture the complicated chemical processes occurring in shales at the transition zone. The transgressive nature of Fuglen shales also implies that there could be depositional trends in the cap rock (i.e., varying silt content). However, the calculated V_S maps significantly underpredict the values encountered at well locations. This observation necessitates revision of the model used for calculation of elastic properties of shales. Nevertheless, V_P and density maps seem to be in good to very good agreement with Backus up-scaled Base Fuglen log values. Moreover, V_S velocities shown in maps in Figures 7 and 8 are irrelevant from

the point of view of the creation of non-stationary AVO PDFs because the generation of V_S random samples (needed for calculation of intercept and gradient attributes via the two-term Shuey equation) is coupled with the creation of V_P random samples via locally established, data-driven V_P - V_S regression coefficients.

In contrast with small differences in elastic properties of shales calculated for two different T_{grad} scenarios, differences in all three elastic parameters for the Stø Fm are substantial in the most buried, bordering areas of the maps, where relatively large quantities of cement material fill the already very stiff sandstone pores. Moreover, V_S velocities, especially for the $T_{\text{grad}} = 38^\circ\text{C}/\text{km}$ case, show values consistent with Gassmann fluid-substituted, brine-saturated values at well locations (in wells that were originally hydrocarbon-saturated). This observation seems to confirm a good understanding of diagenetic processes experienced by siliciclastic rock formations.

Compressional velocity and density values calculated for the Fuglen shales and Stø sand(stone)s for both T_{grad} scenarios served as inputs to the generation of nonstationary AVO PDFs. As explained above, V_S random samples were drawn by considering the locally established V_P - V_S regressions in the aforementioned formations.

Method 3 — Density ratio inversion from Zoeppritz's equation

The method introduced in the previous section falls into a class of forward modeling techniques. In this section, we follow an inversion path suggested by Lehocki et al. (2018), where Zoeppritz's equation (Zoeppritz, 1919) for PP-wave reflection coefficients is studied. This method is mathematically involving and will be presented in detail in a future publication. Here, only the core idea is outlined.

The input parameters to the PP-Zoeppritz equation for plane waves are

$$R_{\text{PP}}(\theta) = R_{\text{PP}}(V_{P1}, V_{S1}, \rho_1, V_{P2}, V_{S2}, \rho_2, \theta), \quad (2)$$

where index 1 refers to layer 1, index 2 refers to layer 2, and θ is the angle of incidence of the plane wave. Two of the parameters are not independent, meaning that equation 2 can be rewritten into a more compressed form, such as

$$R_{\text{PP}}(\theta) = R_{\text{PP}}(AI_r, \rho_r, \gamma_1, \gamma_2, \theta), \quad (3)$$

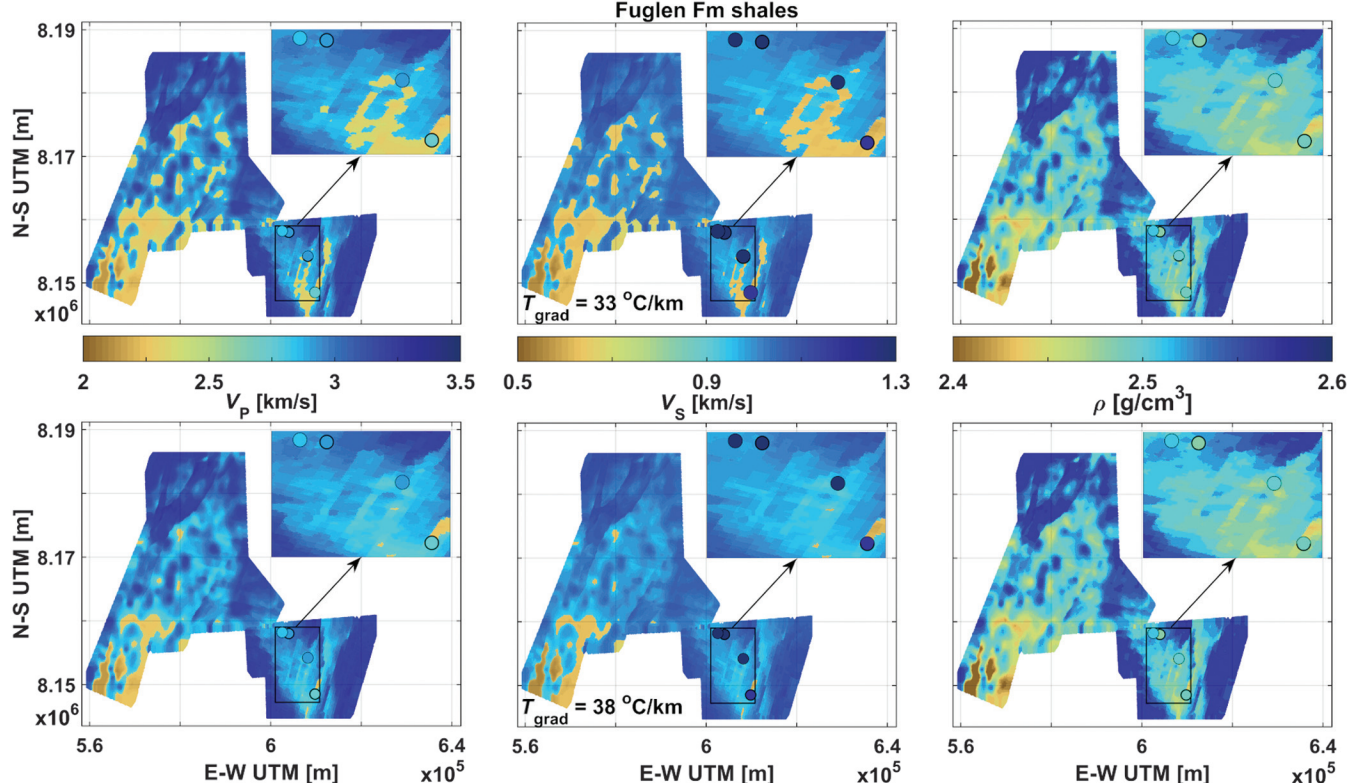


Figure 7. Elastic properties of the Fuglen Fm shales calculated from time trend rock physics modeling for two temperature gradient cases. The $T_{\text{grad}} = 33^{\circ}\text{C}/\text{km}$ case is shown in the upper subplots, and the $T_{\text{grad}} = 38^{\circ}\text{C}/\text{km}$ case is shown in the lower subplots. Note the similarity in the maps and the underestimation of the S-wave velocities in both scenarios.

where the mathematically independent parameters are

$$AI_r = \frac{AI_2}{AI_1}, \quad \rho_r = \frac{\rho_2}{\rho_1}, \quad \gamma_1 = \frac{V_{P1}}{V_{S1}}, \quad \gamma_2 = \frac{V_{P2}}{V_{S2}}. \quad (4)$$

Lehocki et al. (2015) note the following simple relationship:

$$\theta_c = \arcsin\left(\frac{\rho_r}{AI_r}\right). \quad (5)$$

Note that equation 5 expresses a physical principle known as Snell's law, stating that when $V_{P1} < V_{P2}$ (equivalently, $\rho_r < AI_r$), a critical angle θ_c occurs at which the refracted wave rushes along the interface between the two layers. The determination of the density ratio parameter in the ideal case becomes a trivial exercise, given the intercept and critical angle observations. However, the critical angle will move in the presence of anisotropy or if the wavefront curvature is not negligible, as in the case of class I responses (Haase, 2004), or from relatively shallow interfaces (Kralj and Brysk, 1983). Moreover, when the difference between V_{P1} and V_{P2} velocities is small, the critical angles reside in the ultrafar AVA domain ($V_{P1} \leq V_{P2}$), well beyond the range usually collected, or may be nonexistent ($V_{P1} > V_{P2}$). The whole Fuglen shales/Stø sand(stone)s interface exhibits this characteristic, and an example is shown in Figure 4.

To extract the density ratio parameter directly from the PP-Zoeppritz equation, equation 3 can be inverted:

$$\rho_r = \rho_r(AI_r, \gamma_1, \gamma_2, R_{PP}(\theta), \theta). \quad (6)$$

However, the Zoeppritz equations are highly nonlinear and the density ratio is hidden deeply within. As a matter of fact, of all four parameters entering equation 3, this one is by far the most difficult to “excavate” with this (direct inversion) approach. Thus, the inversion of ρ_r from the PP-Zoeppritz equation is an arduous, but not impossible, algebraic task. The inversion leads to a no less than 12th-degree polynomial equation of the form

$$p_{12} \cdot \rho_r^{12} + \dots + p_1 \cdot \rho_r + p_0 = 0 \quad (7)$$

Needless to say, the p_i ($i = 1, \dots, 12$) coefficients are algebraically very complicated. Despite the fearsome look of equation 7, with today’s computational power at disposal, even calculations such as these become tractable. More intriguingly, the solutions for different interfaces are found to be stable; i.e., small fluctuations in the inputs do not change the results significantly. We note that Lehecki et al. (2018) report that a 16th-degree polynomial equation needs to be solved for the density ratio extraction. Although their calculations were correct, they contained redundancies because the four final (consecutive) coefficients can be mathematically reduced to 0.

Note that on the left side of equation 6, the incident angle dependence is deliberately omitted because the density ratio will be the same for each angle of incidence for a particular interface (in ideal, noise-free cases). This opens up the possibility to invert for ρ_r at all angles of interest that are assessed not to be too noisy, distorted by the processing, nor affected by a phenomenon that strongly invalidates the use of the Zoeppritz equation. Thus, a normalized kernel density estimate (NKDE) (see Lehecki et al., 2015) can be constructed from which the most likely, i.e., maximum likelihood (ML), value can be easily calculated. One such calculation is shown in Figure 9.

At first sight, equation 6 suggests that apart from the known AI_r and $R_{PP}(\theta)$, there are two unknown parameters, namely, the V_P/V_S ratios in layers 1 and 2. However, it is shown in Figure 9 on the noise-free shale-sand interface from the Wisting Central well (modeled also in Figure 4) that the knowledge of their particular values is irrelevant from the point of view of the inversion: all that has to be known is the relationship between these two parameters (implicitly contained in the Zoeppritz equation at nonzero angles of incidence) and the maximum of the NKDE will be around the true ρ_r value (note that small errors will arise due to the finite precision of the computations). In other words, the relative frequency of density ratio values comprising the solution space at any nonzero

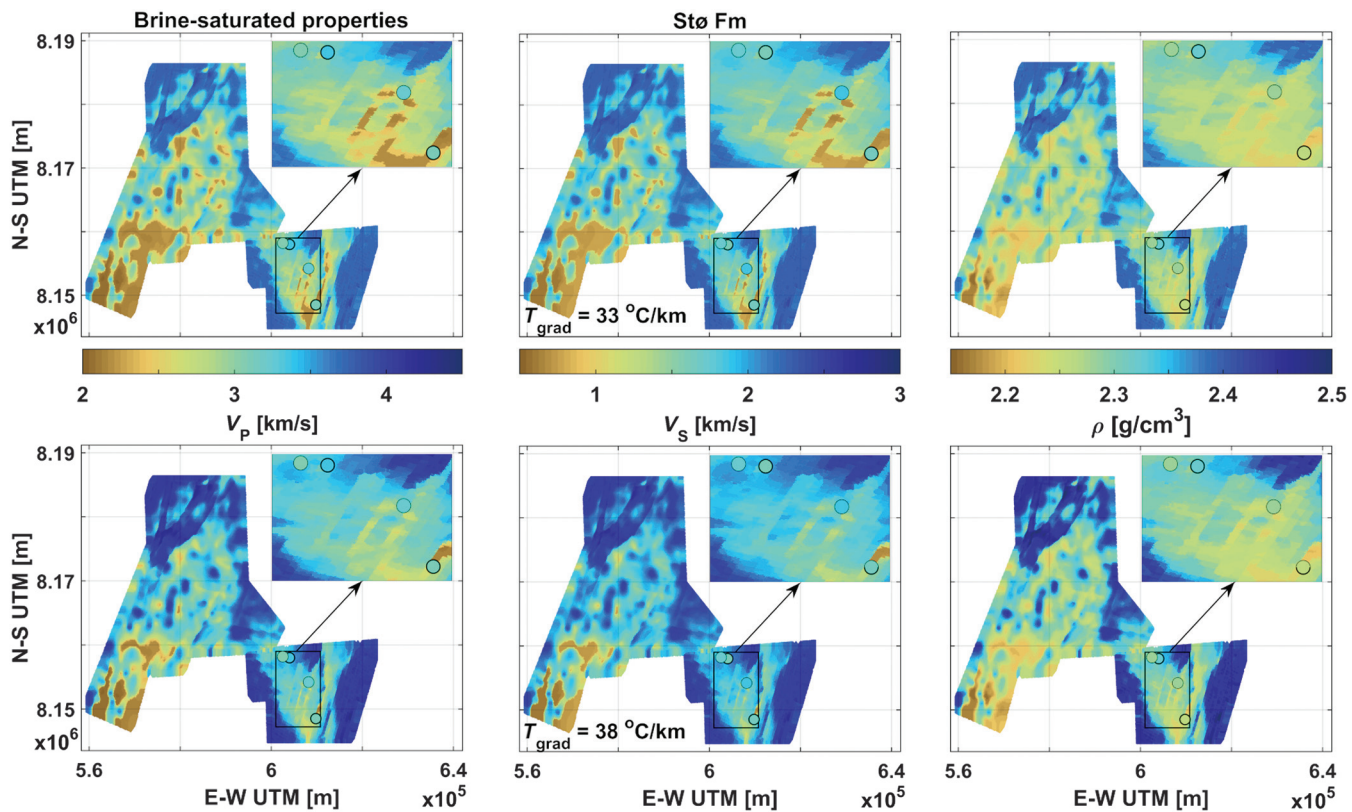


Figure 8. Elastic properties of the Stø Fm brine-saturated sand(stone)s calculated from the time trend rock physics modeling for two temperature gradient cases. The $T_{\text{grad}} = 33^\circ\text{C}/\text{km}$ case is shown in the upper subplots, and the $T_{\text{grad}} = 38^\circ\text{C}/\text{km}$ case is shown in the lower subplots.

incidence angle will be the highest at/around the true solution. However, the shape of any of the three NKDEs reveals a highly complex solution space with multiple sharp and flat local maxima.

Case study — Barents Sea example

The Wisting field is located in the Hoop area in the Barents Sea (Figure 1), and it contains several wells that were drilled into hydrocarbon-saturated reservoir rocks of Middle and Early Jurassic age. Northwest of it lies a prospective area with interesting anomalies (contoured by the black line in Figures 10, 11, and 12). Our goal was to quantitatively assess the fluid distribution at the Fuglen shale-Stø sand(stone) interface from pre-stack gathers and angle stack data with a particular focus on the anomalous zone in the prospective area. Three methods were tested, each with its own set of assumptions.

First, the Zoeppritz inversion procedure for obtaining the most likely density ratio value for a single spatial point from the real data set is described. Due to shallow target, the intercept was extracted not from 0 (or close to 0) angle(s), but from close to mid-angle ranges. Only calibrated intercept and gradient data extracted from two-term Shuey fit to angle stacks up to 40° were used to obtain reflection coefficients in the function of the incidence angle. Because the interface under the scope does not exhibit strong positive intercept values, the curvature term might become important only at ultrafar angles of incidence (as discussed above), well beyond the angle ranges used in this work. Therefore, unnecessary overfitting of the angle stacks is avoided, in accordance with advice from Chopra and Castagna (2014), as the seismic amplitudes in $\sin^2(\theta) \cdot R_{PP}$ plot will be well approximated by the two-term Shuey equation. In other words, curvature attribute extraction is not needed for density information recovery for response classes encountered in this research area. Moreover, a single $\gamma_1\gamma_2$ pair obtained by PP-only AVO inversion (Lehocki and Avseth, 2018) entered equation 6. Finally, density ratio was inverted in the 10° – 40° range with 2° step size. The positive real solution space from all angles considered led to a PDF from which the ML value was calculated. The ML map is shown in the left subplot of Figure 10. This, as well as maps in

Figures 11 and 12, were smoothed by a 5×5 pixel 2D median spatial filter with the goal of suppressing the salt-and-pepper noise. The colors in the color bar reflect

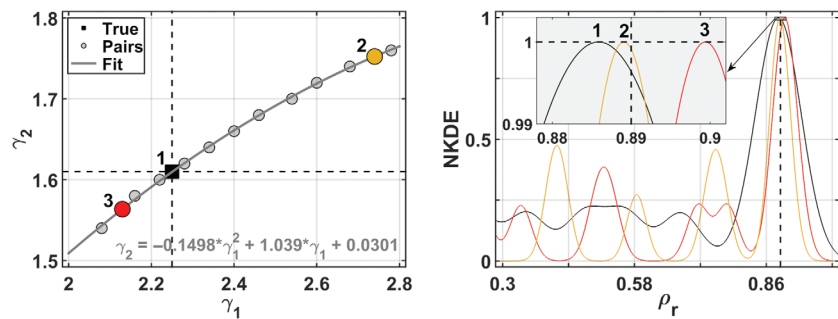


Figure 9. The $\gamma_1\gamma_2$ relationship for the shale-oil sand interface in the Wisting Central well (left) and the 1D NKDE-s calculated in three arbitrary γ_1 points. The intersection of the dashed lines in the left subplot and the vertical line in the right subplot mark the true parameter values.

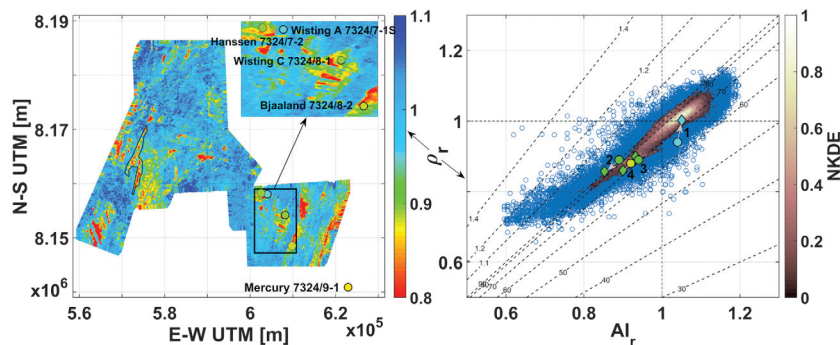


Figure 10. Density ratio map (left) obtained from Zoeppritz's inversion and the corresponding AI_r - ρ_r scatterplot (the blue points in the right subplot). Codes for wells in the right subplot are as follows: 1 — 7324/7-1 S, 2 — 7324/7-2, 3 — 7324/8-1, and 4 — 7324/8-2. The critical angle contours calculated from equation 5 are superimposed and are continued by the ρ_r/AI_r contours beyond the critical angle range. Note that the anomaly (approximately) resides in the $\rho_r/AI_r \geq 1$ domain. Note also from the NKDE that most of the data points lie just around the intersection of the $AI_r = 1$ and $\rho_r = 1$ lines.

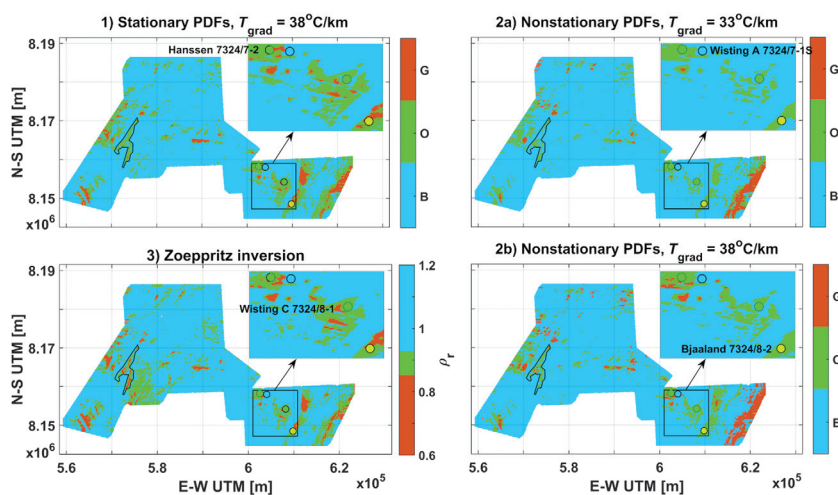


Figure 11. The AVO fluid maps based on the estimated density ratios (lower left) and rock-physics modeling. Note that the Bjaaland well is shown by a yellow circle to reflect the subcommercial (10%–20%) gas content in Stø sand(stone)s.

the most likely pore fluid type (blue — brine, green — oil, red — gas). Furthermore, the subcommercial gas-brine mixture is attempted to be captured by the orange and yellow colors, whereas the transition from oil to brine is marked by the cyan color. Indeed, a close inspection of density ratio values in the vicinity of the Bjaaland well (the magnified part of the map in Figure 10) seems to confirm subcommercial gas saturation, whereas commercial gas fillings might be present in the northeast direction from this well. Moreover, the other three wells are also correctly classified as oil discoveries (Hanssen and Wisting Central) and dry (Wisting Alternative) well. Finally, the anomalous prospective area in the Hoop area (enclosed by the black contour) is probably gas-filled.

The inverted ρ_r values closest to the well positions are summarized in Table 1. Note that they stay within an 8% percentage error of the values observed at well locations. The bulk density values for Fuglen Fm shales

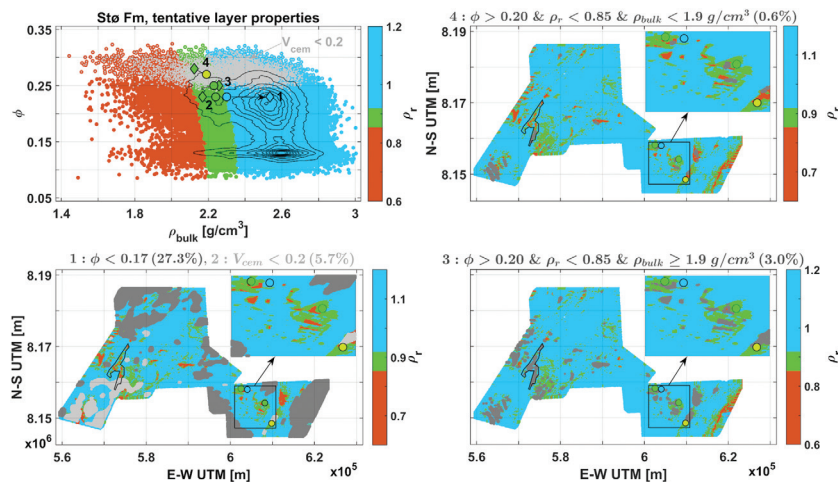


Figure 12. Semiquantitative (uncalibrated) layer properties of the Stø sand(stone)s (the upper left subplot) together with the contours highlighting the largest concentration of the inverted points. The codes for the wells are the same as in Figure 10: 1 — 7324/7-1 S, 2 — 7324/7-2, 3 — 7324/8-1, and 4 — 7324/8-2. Circles denote the averaged values of the uppermost 15 m of Stø sandstone interval from well logs. Diamonds in the bulk density direction mark the values from points closest to the locations of wells obtained from the seismic inversion of density ratios, and in the porosity direction, they mark the values closest to the locations of wells obtained from time trends rock physics modeling. Other subplots highlight areas with specific conditions.

Table 1. Validation of the Zoeppritz's inversion method at well locations.

Method\Well	7324/7-1 S			7324/7-2			7324/8-1			7324/8-2		
Units	[g/cm ³]	[1]										
Parameter	ρ_1	ρ_2	ρ_r	ρ_1	ρ_2	ρ_r	ρ_1	ρ_2	ρ_r	ρ_1	ρ_2	ρ_r
Observed	2.46	2.30	0.94	2.51	2.24	0.89	2.50	2.23	0.89	2.48	2.19	0.88
Calculated	2.51	2.54	1.01	2.52	2.17	0.86	2.51	2.26	0.90	2.47	2.12	0.86
% error	2.00	10.40	7.40	0.40	3.10	3.40	0.40	1.30	1.10	0.40	3.20	2.30

Note: Index 1 refers to Fuglen Fm shales (layer 1), and index 2 denotes Stø Fm sandstones (layer 2). Note that the well 7324/7-1 S shows the highest discrepancies between the observations and the calculations.

were taken from the bulk density values for shales calculated by time trend rock physics modeling (the lower right subplot in Figure 7). Assuming that these are hydrocarbon-free, the bulk density values of the Stø Fm sand(stone)s were calculated by multiplying the bulk density values from Fuglen shales with density ratios obtained from the Zoeppritz inversion. Because density ratios contain information about the fluid type, this information is “transferred” to bulk density values of the Stø Fm. The averaged (blocked) bulk density values observed at the last 15 m of the Fuglen Fm and the first 15 m of the Stø Fm in the wells are also shown for comparison. Note that the calculated Stø Fm bulk density in well 7324/7-1 S is considerably overpredicted compared to the observed value (2.54 g/cm³ versus 2.30 g/cm³, respectively) due to the overprediction of the calculated density ratio value at this point.

A similar color convention is used in Figures 11 and 12 as in Figure 10: Cyan represents brine (B), green corresponds to oil (O), and red depicts gas (G). This time, sharp color boundaries are set between fluids. The results of the three methods are shown in Figure 11. The methods are (in the clockwise direction starting from the upper left subplot):

- 1) Statistical AVO fluid classification with stationary PDFs (obtained with the guidance from the Wisting Central well)
- 2) Statistical AVO fluid classification with nonstationary PDFs for two scenarios:
 - a) $T_{\text{grad}} = 33^\circ\text{C}/\text{km}$
 - b) $T_{\text{grad}} = 38^\circ\text{C}/\text{km}$
- 3) Zoeppritz inversion.

The main observed similarities and/or differences are the following:

- 1) Only methods 2b and 3 give the correct fluid classification for all four wells.

- 2) The down-flank presence of oil associated with some of the predicted gas anomalies in the prospect area is visible only in the case of the Zoeppritz inversion.
- 3) Possible gas caps are detected in the prospective area only on the Zoeppritz inversion map.
- 4) Parts of the Wisting oil field and the prospective area are misclassified as brine points.

Calculations to invert for the density ratio map from the Zoeppritz inversion are computer-intensive, but the advantage is that they are valid as long as the assumptions underlying the isotropic Zoeppritz equation for plane PP-waves are not strongly invalidated. However, the path to creating nonstationary AVO PDFs is considerably longer and there are many more parameters, the values of which need to be fixed. Whereas statistical AVO classification techniques try to account for some of these uncertainties, it is difficult to quantify to which degree it succeeds in doing so. All of these arguments aside, the time trend rock-physics modeling, coupled with the density ratio inversion results, can prove to be extremely useful for creating simple, intuitive, semi-quantitative crossplots of reservoir properties, such as the bulk density-porosity crossplot seen in the upper left subplot of Figure 12. It was created by “borrowing” bulk density values for shales (the lower right subplot in Figure 7) from time trends rock physics modeling. Then, the density values in layer 2 (Stø Fm) were obtained from the density ratio values (as described earlier). Moreover, sand(stone) porosity values were derived from the Ramm and Bjørlykke (1994) empirical models (the lower right subplot in Figure 6).

The word “semiquantitative” in this context means that the absolute locations of inverted points in the upper left crossplot in Figure 12 are incorrect in more cases than not, but their relative locations are correct. As it turns out, when comparing the average porosity values of the uppermost 15 m of Stø sandstones from well logs (circles) with porosity values closest to the locations of wells, Ramm and Bjørlykke’s (1994) empirical modeling coupled with BHCs gives a simple, but powerful tool for prediction/estimation of reservoir porosities. This observation is also supported by a nice match seen in the lower right subplot in Figure 6.

In Figure 12, we present the usefulness of the semiquantitative approach proposed. The upper left subplot shows the calculated reservoir properties of Top Stø Fm sand(stone)s. Then, in the lower left subplot, we highlight the low-porosity areas on the map (case 1 — 27.3% of data have values that satisfy the $\phi < 0.17$ condition — shown in dark gray). Moreover, approximately 6% of unconsolidated sands is expected to be found in the southwest Hoop area (case 2 — $V_{cem} < 0.2$). In subplot 3 (lower right), we highlight points that jointly satisfy three conditions (case 3): porosity of the sands is larger than 0.2, density ratio is smaller than 0.85, and bulk densities are larger than or equal to 1.9 g/cm^3 . This compound condition might correspond to trying to identify

oil or subcommercial gas accumulations in the data. Three percent of data satisfy this criterion and highlight the Wisting and prospective areas. Finally, commercial gas accumulations might be highlighted by changing only the third condition of case 3. Less than 1% of the data (shaded in gray in the upper right subplot in Figure 12) meet this criterion and one part of them resides in the anomalous zone of the prospective area.

Conclusion

We have demonstrated two novel strategies for the estimation of pore fluid distribution in the Stø Fm sand(stone)s in the Hoop area of the southwest Barents Sea. The first method combines information from basin modeling, well log, and prestack seismic data to create geologic, time-dependent, nonstationary AVO PDFs guided by rock-physics modeling to estimate the pore fluid distributions.

The second method involves a direct inversion of the PP-Zoeppritz equation to obtain the density ratio, a very useful parameter for pore fluid detection and subtle pore fluid discrimination. The solution is a 12th-degree polynomial with algebraically complicated coefficients. However, with an ever-increasing computation speed, highly nonlinear AVO inversion techniques are becoming practically applicable. The method is free of empiricism and might potentially be used for density ratio determination for all classes of AVO responses, as long as the angles used in the inversion are restricted to the ranges not affected by other physical phenomena, such as polar anisotropy and/or spherical waves.

The methods have been tested on a hydrocarbon discovery in the Barents Sea. The inverted density ratio values closest to the well locations do not exceed an 8% percentage error. Moreover, both methods correctly classify fluid types at four checkpoint wells. However, only the Zoeppritz inversion method highlights down-flank oil accumulations east of the prospective area. Moreover, possible gas caps are detected in the prospective area, again, only by the Zoeppritz inversion. Subtle, yet important tasks, such as discrimination between low gas and commercial gas saturations, seem to be possible from the inverted density ratio parameter, even in (initially) cemented rocks. The reason is that the masking effects on elastic properties caused by the diagenetic cement leave the rock’s bulk density largely (however, not completely) unaltered/unaffected.

Finally, by combining results from Zoeppritz’s inversion and geologic time-trends rock-physics modeling, the possibility to make a semiquantitative bulk density-total porosity crossplot of the target Stø Fm sand(stone)s opens up. This allows for a quick and simple qualitative assessment of the reservoir conditions, such as the diagnosis of the degree of consolidation/diagenesis and reservoir texture.

Acknowledgments

We are thankful to the OMV w/partners (PL 537) and TGS (data owner) for allowing us to publish the AVO

data used in this study. We also thank F. Larsson and R. Manafov, formerly at Moeco Oil & Gas Norge AS, for their valuable input to this work.

Data and materials availability

Data associated with this research are confidential and cannot be released.

References

- Alkawai, W. H., T. Mukerji, A. H. Scheirer, and S. A. Graham, 2018, Integrating statistical rock physics and pressure and thermal history modeling to map reservoir lithofacies in the deepwater Gulf of Mexico: *Geophysics*, **83**, no. 4, IM15–IM28, doi: [10.1190/geo2017-0427.1](https://doi.org/10.1190/geo2017-0427.1).
- Avseth, P., H. Flesche, and A.-J. van Wijngaarden, 2003, AVO classification of lithology and pore fluids constrained by rock physics depth trends: *The Leading Edge*, **22**, 1004–1011, doi: [10.1190/tle35060528.1](https://doi.org/10.1190/tle35060528.1).
- Avseth, P., and I. Lehocki, 2016, Combining burial history and rock-physics modeling to constrain AVO analysis during exploration: *The Leading Edge*, **35**, 528–534, doi: [10.1190/tle35060528.1](https://doi.org/10.1190/tle35060528.1).
- Baig, I., J. I. Faleide, J. Jahren, and N. H. Mondol, 2016, Cenozoic exhumation on the southwestern Barents Shelf: Estimates and uncertainties constrained from compaction and thermal maturity analyses: *Marine and Petroleum Geology*, **73**, 105–130, doi: [10.1016/j.marpetgeo.2016.02.024](https://doi.org/10.1016/j.marpetgeo.2016.02.024).
- Bjørlykke, K., 1998, Clay mineral diagenesis in sedimentary basins — A key to the prediction of rock properties. Examples from the North Sea Basin: *Clay Minerals*, **33**, 15–34, doi: [10.1180/000985598545390](https://doi.org/10.1180/000985598545390).
- Bjørlykke, K., 2015, Petroleum geoscience: From sedimentary environments to rock physics: Springer, 662.
- Chopra, S., and J. P. Castagna, 2014, AVO: SEG, Investigations in Geophysics 16.
- Dræge, A., K. Duffaut, T. Wiik, and K. Hokstad, 2014, Linking rock physics and basin history — Filling gaps between wells in frontier basins: *The Leading Edge*, **33**, 240–246, doi: [10.1190/tle33030240.1](https://doi.org/10.1190/tle33030240.1).
- Farazani, N., 2017, Reservoir quality of the Stø Formation in the Hoop Fault Complex and Fingerdjupet Sub-basin, SW Barents Sea (The transition between the Stø and Fuglen Formations): Master's thesis, doi: [10.13140/RG.2.2.10436.94081](https://doi.org/10.13140/RG.2.2.10436.94081).
- Gateman, H., and P. Avseth, 2016, Net uplift estimation using both sandstone modeling and shale trends, on the Horda Platform area in the Norwegian North Sea: 86th Annual International Meeting, SEG, Expanded Abstracts, 3288–3292, doi: [10.1190/segam2016-13865497.1](https://doi.org/10.1190/segam2016-13865497.1).
- Haase, A. B., 2004, Spherical wave AVO modeling of converted waves in isotropic media: 74th Annual International Meeting, SEG, Expanded Abstracts, 263–266, doi: [10.1190/1.1851262](https://doi.org/10.1190/1.1851262).
- Henriksen, E., H. M. Bjørnseth, T. K. Hals, T. Heide, T. Kiryukhina, O. S. Kløvjan, G. B. A. E. Larssen, K. Ryseth, K. Rønning, Sollid, and A. Stoupakova, 2011, Chapter 17: Uplift and erosion of the greater Barents Sea: Impact on prospectivity and petroleum systems: Geological Society, London, Memoirs 35, 271–281.
- Johansen, N., P. Avseth, K. Duffaut, and M. B. Mørk, 2017, Burial history and implications for seismic AVO signatures in the Western Barents Sea: 4th International Rock Physics Workshop.
- Khutorskoi, M. D., K. G. Viskunova, L. V. Podgornyykh, O. I. Suprunenko, and V. R. Akhmedzyanov, 2008, A temperature model of the crust beneath the Barents Sea: Investigations along geotraverses: *Geotectonics*, **42**, 125–136, doi: [10.1134/S0016852108020039](https://doi.org/10.1134/S0016852108020039).
- Krali, P. M., and H. Brysk, 1983, Reflection of spherical seismic waves in elastic layered media: *Geophysics*, **48**, 655–664, doi: [10.1190/1.1441496](https://doi.org/10.1190/1.1441496).
- Lehocki, I., and P. Avseth, 2018, AVO inversion using physical constraints: 80th Annual International Conference and Exhibition, EAGE, Extended Abstracts, doi: [10.3997/2214-4609.201801538](https://doi.org/10.3997/2214-4609.201801538).
- Lehocki, I., P. Avseth, and V. Hadžiačkić, 2015, Probabilistic estimation of density and shear information from Zoepritz's equation: *The Leading Edge*, **34**, 1036–1038, 1040, 1042, 1044, 1046–1047, doi: [10.1190/tle34091036.1](https://doi.org/10.1190/tle34091036.1).
- Lehocki, I., P. Avseth, F. Larsson, and R. Manafov, 2018, Exploring Zoepritz for more constrained and reliable density ratio estimation: 88th Annual International Meeting, SEG, Expanded Abstracts, 580–584, doi: [10.1190/segam2018-2998598.1](https://doi.org/10.1190/segam2018-2998598.1).
- Lewis, O. J., P. Smith, M. Hohner, T. Kvist-Lassen, L. Dahlhaus, L. Stuberg, J. R. Granli, H. Veire, and P. Berger, 2016, Integrated processing of borehole and surface seismic measurements for enhanced well tie and AVO analysis: 78th Annual International Conference and Exhibition, EAGE, Extended Abstracts, doi: [10.3997/2214-4609.201601553](https://doi.org/10.3997/2214-4609.201601553).
- Ramm, M., and K. Bjørlykke, 1994, Porosity/depth trends in reservoir sandstones assessing the quantitative effects of varying pore-pressure, temperature history and mineralogy, Norwegian Shelf data: *Clay Minerals*, **29**, 475–490.
- Smith, G. C., and P. M. Gidlow, 1987, Weighted stacking for rock property estimation and detection of gas: *Geophysical Prospecting*, **35**, 993–1014, doi: [10.1111/j.1365-2478.1987.tb00856.x](https://doi.org/10.1111/j.1365-2478.1987.tb00856.x).
- Veire, H., J. R. Granli, P. Berger, O. Lewis, M. Hohner, T. Kvist-Lassen, P. Smith, and L. Stuberg, 2016, The Wisting discovery — Integrating acoustic measurements at different scales: 78th Annual International Conference and Exhibition, EAGE, Extended Abstracts.
- Zattin, M., B. Andreucci, B. de Toffoli, D. Grigo, and F. Tsikalas, 2016, Thermochemical constraints to late Cenozoic exhumation of the Barents Sea Shelf: *Marine and Petroleum Geology*, **73**, 97–104, doi: [10.1016/j.marpetgeo.2016.03.004](https://doi.org/10.1016/j.marpetgeo.2016.03.004).
- Zoeppritz, K., 1919, Erdbebenwellen VIIIB, Über Reflexion und Durchgang seismischer Wellen durch Unstetigkeitsflächen: *Goettinger Nachrichten* I, 66–84.



Ivan Lehocki received an M.S. in geophysics from the Eötvös Loránd University, Budapest, Hungary; in space science and technology from the Luleå University of Technology, Luleå, Sweden; and in astrophysics, space science, and planetology from Paul Sabatier University, Toulouse, France. He is a senior software developer at Lehocki GeoSpace, Oslo, Norway. His main research interests are within quantitative seismic interpretation.



Per Avseth received an M.S. (1994) in applied petroleum geosciences from the Norwegian University of Science and Technology (NTNU) and a Ph.D. (2000) in geophysics from Stanford University, California. He is the lead geophysicist and CTO at Dig Science in Oslo, Norway, and an adjunct professor in reservoir geophysics at NTNU in Trondheim, Norway. He worked as a research geophysicist at Norsk Hydro in Bergen (2001–2006), he was a consultant at Rock Physics Technology (2006–2008) and Odin Petroleum (2008–2012) in Bergen, Norway, and he

was a geophysical advisor at Tullow Oil Norway in Oslo (2012–2016). His research interests include applied rock physics, AVO analysis, and machine learning for quantitative seismic exploration, basin analysis, and reservoir characterization.



Nazmul Haque Mondol received a B.S. in geology from the University of Dhaka, Bangladesh, an M.S. in geology from the University of Dhaka, Bangladesh, an M.S. in petroleum geosciences from the Norwegian University of Science & Technology, Norway, and a Ph.D. in experimental rock physics from the University of Oslo, Norway.

He is a professor at the University of Oslo and an advisor (adjunct position) at NGI, Oslo, Norway. He was a postdoctoral fellow at the University of Oslo, Norway (with grants from the Research Council of Norway under the PETRO-MAKS program), before permanently joining the University of Oslo. His research interests include rock physics, petrophysics, geophysics, geomechanics, geology, and seismic to characterize the source, reservoir, cap, and overburden rocks for exploration and exploitation of conventional and unconventional hydrocarbon resources, and geological storage of CO₂.